

See discussions, stats, and author profiles for this publication at: <https://www.researchgate.net/publication/312202084>

# Multifunctional metal matrix composites with embedded printed electrical materials fabricated by Ultrasonic Additive...

Article *in* Composites Part B Engineering · January 2017

DOI: 10.1016/j.compositesb.2017.01.013

---

CITATIONS

2

READS

60

6 authors, including:



[Tho T. Nguyen](#)

The Welding Institute (TWI)

11 PUBLICATIONS 14 CITATIONS

[SEE PROFILE](#)



[Robert W. Kay](#)

University of Leeds

68 PUBLICATIONS 276 CITATIONS

[SEE PROFILE](#)

Some of the authors of this publication are also working on these related projects:



Manufacturing with Light 2: Photobioform II [View project](#)

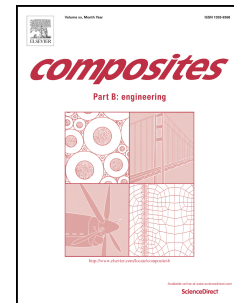


Full-field property characterisation of non-homogeneous materials by the Fourier Virtual Fields Method  
[View project](#)

# Accepted Manuscript

Multifunctional metal matrix composites with embedded printed electrical materials fabricated by Ultrasonic Additive Manufacturing

J. Li, T. Monaghan, T.T. Nguyen, R.W. Kay, R.J. Friel, R.A. Harris



PII: S1359-8368(16)31839-X

DOI: [10.1016/j.compositesb.2017.01.013](https://doi.org/10.1016/j.compositesb.2017.01.013)

Reference: JCOMB 4824

To appear in: *Composites Part B*

Received Date: 16 August 2016

Revised Date: 19 December 2016

Accepted Date: 8 January 2017

Please cite this article as: Li J, Monaghan T, Nguyen TT, Kay RW, Friel RJ, Harris RA, Multifunctional metal matrix composites with embedded printed electrical materials fabricated by Ultrasonic Additive Manufacturing, *Composites Part B* (2017), doi: [10.1016/j.compositesb.2017.01.013](https://doi.org/10.1016/j.compositesb.2017.01.013).

This is a PDF file of an unedited manuscript that has been accepted for publication. As a service to our customers we are providing this early version of the manuscript. The manuscript will undergo copyediting, typesetting, and review of the resulting proof before it is published in its final form. Please note that during the production process errors may be discovered which could affect the content, and all legal disclaimers that apply to the journal pertain.

# Multifunctional Metal Matrix Composites with Embedded Printed Electrical Materials Fabricated by Ultrasonic Additive Manufacturing

J. Li<sup>1,2,\*</sup>, T. Monaghan<sup>2</sup>, T.T. Nguyen<sup>2</sup>, R.W. Kay<sup>3</sup>, R.J. Friel<sup>2</sup>, R.A. Harris<sup>3</sup>

Email: [j.li5@seu.edu.cn](mailto:j.li5@seu.edu.cn); [J.Li5@Lboro.ac.uk](mailto:J.Li5@Lboro.ac.uk) Tel: +44(0)1509227567

<sup>1</sup> Key Laboratory of MEMS of the Ministry of Education, Southeast University, Nanjing, 210096, China.

<sup>2</sup> Wolfson School of Mechanical and Manufacturing Engineering, Loughborough University, Loughborough, Leicestershire, LE11 3TU, UK

<sup>3</sup> Mechanical Engineering, University of Leeds, Leeds, LS2 9JT, UK

## Abstract

This work proposes a new method for the fabrication of Multifunctional Metal Matrix Composite (MMC) structures featuring embedded printed electrical materials through Ultrasonic Additive Manufacturing (UAM). Printed electrical circuitries combining conductive and insulating materials were directly embedded within the interlaminar region of UAM aluminium matrices to realise previously unachievable multifunctional composites. A specific surface flattening process was developed to eliminate the risk of short circuiting between the metal matrices and printed conductors, and simultaneously reduce the total thickness of the printed circuitry. This acted to improve the integrity of the UAM MMC's and their resultant mechanical strength. The functionality of embedded printed circuitries was examined via four-point probe measurement. DualBeam Scanning Electron Microscopy (SEM) and Focused Ion Beam (FIB) milling were used to investigate the microstructures of conductive materials to characterize the effect of UAM embedding energy whilst peel testing was used to quantify mechanical strength of MMC structures in combination with optical microscopy. Through this process, fully functioning MMC structures featuring embedded insulating and conductive materials were realised whilst still maintaining high peel resistances of ca. 70 N and linear weld densities of ca. 90%.

Keywords: Ultrasonic additive manufacturing; Metal matrix composites (MMCs); 3D Printing; Embedded electrical circuitry; Mechanical testing; Electron microscopy;

## 1. Introduction

Multifunctional Additive Manufacturing (MAM) is now becoming an important research area in the Additive Manufacturing (AM)/3D Printing (3DP) arena. Unlike traditional AM processes, which mostly deal with mono-functional homogenous structures, MAM combines different types of AM processes to enable the fabrication of novel structures capable of providing high end-use

---

\* Corresponding author.

functionality, complex structures and multiple material combinations. This affords greater versatility of design and manufacturing.

Earlier works in this area were developed by Weiss and Prinz via Shape Deposition Manufacturing (SDM) [1–3]. They demonstrated a 3D printed, waterproof and wearable computer with embedded electronics relevant to military applications. Wicker's group employed Stereolithography (SLA) together with Direct-Writing (DW) to build 3D electronic structures [4–7]. They also combined DW with Fused Deposition Modelling (FDM) to fabricate more robust 3D electronic devices [8]. The MAM technologies mentioned above were based on the fabrication of polymer-based products. The lower resistance to thermal and mechanical stress is a consideration to the application of these polymer-based components. Therefore, some MAM solutions dealing with metallic materials have been proposed. Li et al. integrated fibre optic sensors and thin film sensors within metallic structures via laser assisted SDM [9–11]. Similar fibres were also embedded into metal parts by Maier et al. via Selective Laser Melting (SLM) [12]. Although these methods did provide multifunctional metal structures, special measures were required to protect delicate electronic components from harsh processing environments (e.g. high processing temperatures, large residual stress). This requirement acts to increase the complexity of the manufacturing process. Comparatively, Ultrasonic Additive Manufacturing (UAM) appears to be a viable alternative to previous methods employed due the unique abilities associated with this solid state fabrication process and limited temperature experienced [13].

Ultrasonic Additive Manufacturing (UAM) applies Ultrasonic Metal Welding (UMW) to weld metal foils layer by layer, and intermittent Computer Numerical Control (CNC) machining to create three-dimensional structures [14] (Fig. 1). During this process, a rolling sonotrode exerts a normal compressive force and ultrasonic oscillations to a thin metallic foil (typically 50–300 µm thick). The friction induced at the mating interface between the foil and substrate, in combination with the plastic deformation of the metal adjacent to the contacting points, disrupts the surface oxide layer and creates direct metal-to-metal connections. This results in true metallurgical bonding at the metal to metal interface [15]. Three control parameters: normal force (N) of sonotrode, amplitude of oscillation (µm), and welding speed (mm/s) can be varied by users to adjust the welding energy applied to the work piece. Since the bulk temperature UAM process temperatures do not exceed one half of the melting temperature of the matrix, various alloys such as NiTi and FeGa, and polymers such as PVDF, have been successfully embedded without degradation of the smart material or the matrix. This

Two unique factors of UAM enable the embedment of a wide range of components into metal matrices. Firstly, the bulk temperature of the work piece during UAM process is less than half that of the melting point of the processed metals [16]. This acts to minimise potential thermal damage to vulnerable embedded components[17]. Secondly, a relatively large plastic metal flow, driven by ultrasonic welding, allows the fully embedding of functional components [18]. To date, various elements such as shape memory alloy (SMA) fibers [19–22], optical fibres [23,24], pre-packaged electronic systems [25], direct-written circuitries [26], magnetostrictive Galfenol [20–

22], electroactive PVDF film [21], and electrical switches made of shape memory nickel-titanium (Ni-Ti) [27] have been successfully embedded within UAM metal components.

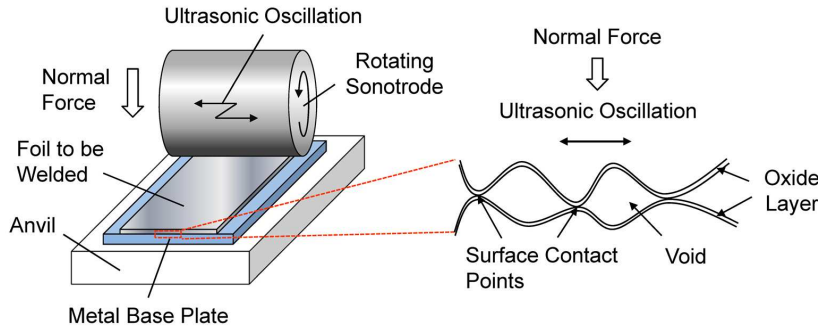


Fig. 1. Schematic drawing of Ultrasonic Additive Manufacturing (UAM) (adapted from Figure 1. of [28]).

Despite its advantages, there are still issues associated with the embedding of electronic structures via UAM: (1) most current works are still restricted to 2D electronic embedding. This lack of 3D capability restricts the potential scope of applications for this technology; (2) the size of embedded electronics are relatively large, which adversely effects not only the structural integrity of the MMC but also the mechanical strength of the UAM structure; (3) extra steps such as CNC milling of protection cavity and filling with secondary protective materials make the manufacturing process much more complex. Therefore, it is pertinent to explore innovative technologies that may realise multifunctional metal matrix composite (MMC) via direct UAM embedding of printed electronics within metal matrices.

This paper focuses on the direct UAM embedding of printed electrical circuitries (insulators and conductive traces) within metal matrices via a combination of screen printing and a specific surface flattening process. The effects of the UAM process on the electrical functionality of printed circuitry were systematically investigated by means of four-point probe measurement and focus variation microscopy. Micro-structure variations of printed conductive material due to UAM embedment were identified via a DualBeam (Focused Ion Beam (FIB) and Scanning Electron Microscope (SEM)) Microscope System. The mechanical strength of the UAM MMC was then explored through a combination of optical microscopy and mechanical peel testing. As a result of the information gained in this study, we are able to report the first instance of directly embedded printed electrical circuitry via UAM without the requirement for pre-fabricated pockets or additional protection. This is a vital step towards realising smart metal components with integrated freeform electrical circuitry for future industrial applications.

## 2. Methodology

### 2.1. Materials

Aluminium (Al) 1050 H14 plate, 5 mm thick and 30 mm wide was used as a base plate for the UAM process. Al 3003 H18 foils with a thickness and a width of ~100  $\mu\text{m}$  and 24 mm respectively were adopted as the matrix material and welded onto the Al 1050 base plate.

For the printed circuitry, 520 Series Soldermask from Technic (Technic Inc., Cranston Rhode Island, USA) [29] was previously demonstrated to be highly compatible with the UAM process [30], and thus was chosen as the electrical insulation material. Isotropically Conductive Adhesives (ICAs) composing of resin binders and conductive fillers were employed to make conductors due to the advantages of superior environmental friendliness, lower processing temperatures, and simpler processing steps [31]. A serials of materials such as; silver (Ag), gold (Au), copper (Cu), and carbon (C) can be used as conductive fillers in ICAs. Due to its higher electrical conductivity, Ag is the most popular choice of conductive filler. Moreover, Ag has superior conductivity stability by the nature of its conductive oxide ( $\text{Ag}_2\text{O}$ ) and thus, silver based ICAs normally show improved electrical conductivity when exposed to high temperature (up to ca. 200°C) and high humidity environments [32]. Two common formats of conductive fillers are flake and particle. It was unknown if these different formats would provide different conductive performance and mechanical strength. Accordingly, two printable silver inks made by Gwent Group (Gwent Electronic Materials Ltd, Pontypool, UK), C2050712P58 (P58, flake) and C2131014D3 (4D3, particle), were intentionally selected as conductive materials for trial. The properties and processing conditions of the two silver inks from manufacturers are state in Table 1 [33,34].

Table 1. Product properties and processing parameters of printable inks.

	C2050712P58 Silver ink	C2131014D3 Silver ink
Type	Single-component	Single-component
Filler	Silver flakes	Silver particles
Solids content (at 700 °C)	58.85 wt% (Silver flakes)	58.85 wt% (Silver particles)
Filler Size	The diameter of 90% of the conductive flakes is less than 21 $\mu\text{m}$ .	The diameter of 90% of the conductive particles within the ink are less than 19.7 $\mu\text{m}$ .
Cure conditions (Box oven)	130 °C/30 min	130 °C/10 min
Volume resistivity	$7.5 \times 10^{-5} \Omega\cdot\text{cm}$	$2.5 \times 10^{-4} \Omega\cdot\text{cm}$

## 2.2. Process chain

The process chain for building the described multifunctional MMC's via UAM can be divided into three stages: (1) UAM substrate fabrication, (2) circuitry printing, and (3) UAM embedding. In the first stage, two Al 3003 H18 foils were ultrasonically welded individually onto an Al 1050 H14 base plate by Alpha 2 machine (Solidica Inc., Ann Arbor, USA) at room temperature (Fig. 2 (a)). The UAM parameters were set at 1600 N normal force, 25  $\mu\text{m}$  sonotrode amplitude, and 20 mm/s welding speed. These parameters were obtained via systematic tests and prior studies focusing on the UAM of 3003 H18 aluminium foils [16,35,36]. The impingement of the sonotrode during UAM processing produces a significantly rough texture on the top surface of the welded foil. According to preliminary testing performed in this work, to enable appropriate functionality of the printed conductors, at least two layers of insulation material (ca. 40  $\mu\text{m}$ ) must be deposited onto this surface in order to overcome the rough inter-UAM foil surface geometry and eliminate electrical shortages between the UAM metal matrices and the conductors. The requirement to deposit these additional layers led to an increase in the total thickness of electrical components, thereby reducing the integrity of the overall structure. Thus, a flattening process was developed in order to reduce the roughness of the UAM processed surface and thus enable a thinner base insulation layer to be used to provide reliable electrical insulation and eliminate short circuiting. Consequently, the total thickness of printed circuitry is supposed to be reduced from ~80  $\mu\text{m}$  to ~60  $\mu\text{m}$  which improved the integrity of the UAM MMC. A titanium alloy foil (Ti-6Al-4V, ~50  $\mu\text{m}$  thick) was placed on the top surface of the UAM processed substrate, and the sonotrode rolled along the titanium alloy foil at 1600 N force and 10 mm/s speed. The relatively high sonotrode pressure and low processing speed adopted in the flattening is expected to achieve obvious deformation of the substrate surface due to the plasticity nature of metal.

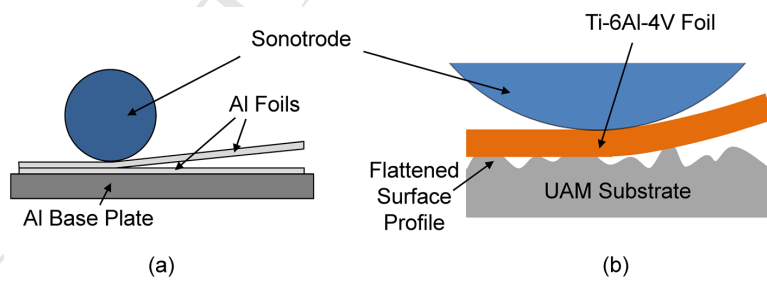


Fig. 2. Aluminium substrate fabrication via UAM process.

The second stage was the printing of electrical circuitry onto the substrate surface. Screen printing was used to deposit electrical materials due to its fast speed, high reliability and its compatibility with the chosen electrical materials. Insulation and conductive materials were sequentially printed onto UAM substrates using a DEK 265 Horizon printer with a mesh screen and bespoke stencil (Fig. 3 (a)). Conductors with two different line widths, 400  $\mu\text{m}$  and 500  $\mu\text{m}$ , were printed and tested in this work. Conductors with 200  $\mu\text{m}$  and 300  $\mu\text{m}$  line widths were also explored for this work, however there were issues with the production of continuous conductive

pathways at these narrower widths. It was hypothesised that this was due to the slightly protruding nature of the insulator adversely affecting the screen printing of the tracks. These small surface imperfections were not an issue in the thicker tracks which produced conductive pathways with high degrees of repeatability. The printed inks were then cured as recommended by the manufacturers and the design dimensions of the printed circuitry are shown in Fig. 3 (b).

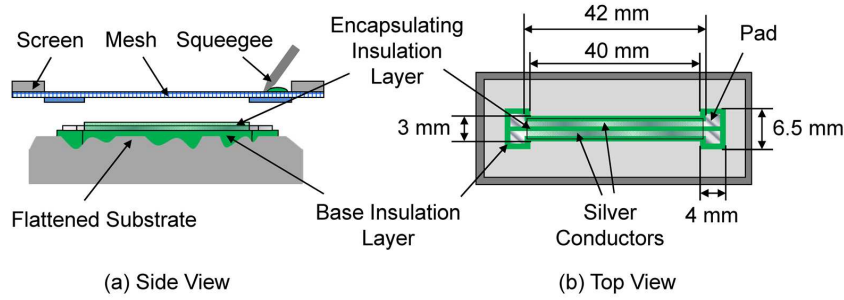


Fig. 3. Electrical circuitry printing using screen printing process.

In the third stage, the printed circuitry was embedded via the ultrasonic welding of an encapsulating Al 3003 H18 covering foil onto the UAM substrate (Fig. 4). Two parameter combinations for this encapsulating were employed: a high UAM energy combination (1600 N normal force, 25  $\mu\text{m}$  sonotrode amplitude, and 20 mm/s welding speed) and a low UAM energy set (800 N normal force, 15  $\mu\text{m}$  sonotrode amplitude, and 10 mm/s welding speed). According to an analytical energy model proposed by Yang et al. [37], the energy density of high and low UAM energy combinations is  $2 \text{ J/mm}^2$  and  $1.2 \text{ J/mm}^2$ , respectively. Thus, the potential effect of UAM embedding energy on embedded circuitries and the mechanical strength of the resultant MMC could be identified. Reference monolithic samples with no printed circuitry were also manufactured with both UAM parameter sets to evaluate any potential change of mechanical strength caused by the circuitry embedment.

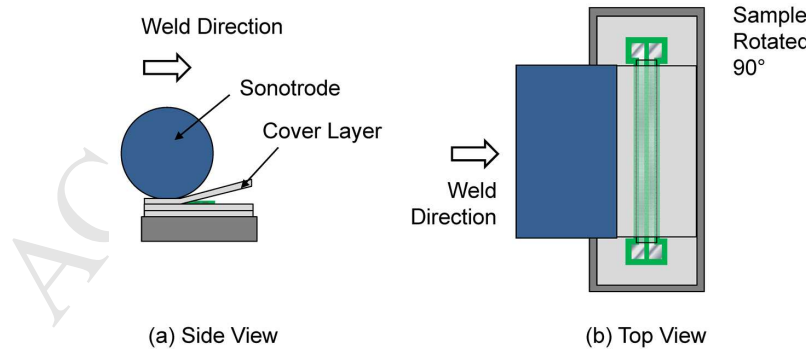


Fig. 4. Printed circuitry embedding via UAM.

### 2.3. Topography analysis

An Alicona InfiniteFocus® G4f non-contact focus variation microscopy system was used to obtain both the surface morphologies of original and flattened UAM substrates and the profiles of printed circuitries. This method could identify any modification of UAM substrate topography due to the flattening process and the geometric profile of the printed circuitries. By comparing the surface profile of the UAM substrate and the thickness of base insulation film, it could be verified that the base insulation layer was thick enough to overcome the surface roughness of the UAM processed substrate and ensure reliable electrical insulation. Furthermore, the profile data of printed conductors were employed for the calculation of the resistivity of the conductors in section 2.4.

For surface morphology of UAM substrate, an object lens with 20 times magnification was utilised. This magnification provides high enough sensitivity to yield topographical information for surface roughness values such as those displayed in UAM substrates. This method has been used in previous works for similar measurements [38]. For each type of substrate (unflattened and flattened) three individual samples were investigated and three scanning areas taken at randomly selected points along the central line of each sample.

For the profiles of printed circuits, the  $\times 10$  object lens employed as this magnification is well suited to step height measurements where there is no need for intense surface measurements. For both the base insulation film and completed circuitry, four samples were measured and three scanning areas were adopted from right, middle, and left part of each sample (twelve scans in total) (Fig. 5(a)). This methodology was again repeated on the conductive tracks with three scanning areas along the length of the silver ink (Fig. 5(b)). For both silver inks and both line widths, twenty-four conductors were investigated and thus seventy-two regions were scanned.

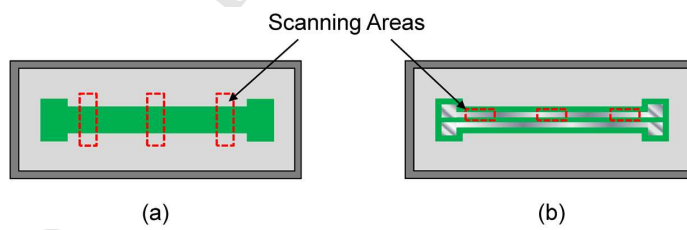


Fig. 5. Scanning area arrangements for investigating the profiles of printed circuitries.

### 2.4. Effects of UAM embedment on the conductivity of printed conductors

#### 2.4.1 Resistivity of printed conductors

To verify any effects of the UAM embedding process on the functionality of the embedded circuitries, the resistivity of the printed conductors was established both before and after UAM embedding.

Four-point probe measurements were performed to measure the electrical resistance of the whole printed conductors using a Keithley 580 Micro-ohmmeter (Keithley Instruments Inc., Ohio, USA). By passing a current through the conductor and measuring the resulting voltage drop across the conductor allowed the measurement of the resistance on the basis of Ohm's law.

According to Pouillet's law, the resistance of a conductor  $R$  ( $\Omega$ ) is expressed as the following equation:

$$R = \rho \frac{L}{A} \quad (1)$$

Where  $\rho$  ( $\Omega \cdot \text{cm}$ ) is the resistivity,  $L$  (cm) is the length of the conductor and  $A$  ( $\text{cm}^2$ ) is the cross-section area of the conductor. For a conductor that has a uniform cross section with a uniform flow of electric current, and is made of one material, the resistance of a section of the conductor can therefore be described using the following equation:

$$R' = \frac{l'}{L} R \quad (2)$$

where  $R'$  ( $\Omega$ ) and  $l'$  (cm) are the resistance and the length of the section, respectively.

However, for the printed conductors, the cross-sectional area varied along the transverse direction due to the screen printing process and thermal curing of the conductive silver ink. The resulting cross-sectional area fluctuation could be characterised and compensated for by the Alicona scanning files of the representative sections measured, as described in Section 2.3. The Alicona scanning files were a matrix of data points with three dimensional coordinate values, and thus a series of cross-section profiles of the conductor could be extracted from the files (Fig. 6(b)). The scanned section then could be regarded as a combination of tiny parts that separated by the cross-section profiles as shown in Fig. 6(a). Thus, the resistance of the scanned section could be calculated via summarizing the resistance of all the individual parts as:

$$R' = \sum_{i=0}^{n-1} R_i = \sum_{i=0}^{n-1} \rho \frac{l}{A_i} = \rho l \sum_{i=0}^{n-1} \frac{1}{A_i} \quad (3)$$

where  $\rho$  ( $\Omega \cdot \text{cm}$ ) is the resistivity,  $l$  (cm) equal distance between cross-section profiles,  $n$  is the number of cross-section profiles and  $A_i$  ( $\text{cm}^2$ ) is the cross-sectional area of the conductor.

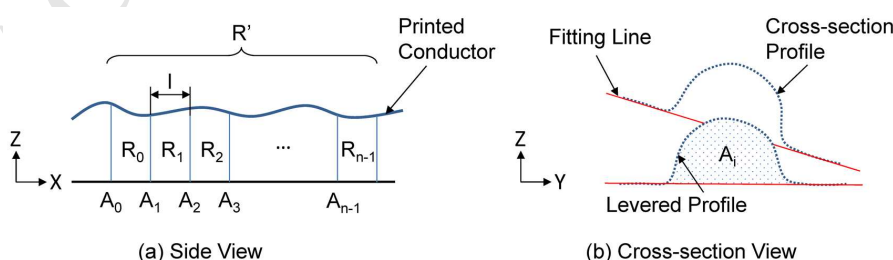


Fig. 6. Schematic drawing of the calculation method for the resistance of scanned conductor

section.

By inserting Eq. (2) into Eq. (3), the resistivity of the scanned section could be described as:

$$\rho = \frac{l' R}{L l \sum_{i=0}^{n-1} \frac{1}{A_i}} \quad (4)$$

As the printed conductor was made of a single homogenised conductive ink material, the resistivity of the scanned section can be regarded as the resistivity of the whole conductor.

A MATLAB® program based upon Random Sample Consensus (RANSAC) [39] was written to extract cross-section profiles and implement the computation of the resistivity of the printed tracks. RANSAC was applied to the flatter portions of the scanned profile (Fig. 6(b)) and a line of best fit through these points included. The fitting line, together with the dataset, was adjusted to be horizontal and then levelled to zero. The cross-sectional area of the conductive tracks was then determined by the region between the curved portion of the profile and the horizontal axis.

#### 2.4.2 FIB investigation

To investigate any possible physical effects of the UAM embedding process on the resistivity/microstructure of the silver conductors, a Focussed Ion Beam (FIB) Scanning Electron Microscope (SEM) DualBeam Microscope System (Nova 600 Nanolab Dual Beam from FEI) was used. The system consists of a high resolution field emission electron column and gallium ion source column, combined within the same instrument. This combination allows milling of cross sections through samples and subsequent imaging using either electrons or ions with the materials remaining unchanged and in situ.

All substrates used in this analysis were manufactured as outlined in Section 2.2. These samples were cross-sectioned in the central region of the conductive track, mounted in an epoxy resin and finally ground and polished to a 0.05 µm finish. Ion beam milling was then used to produce a 20 µm wide, 25 µm long and 20 µm deep trench parallel to the print direction of the conductive silver ink and directly encompassing the entire track cross section. Once milled, the interface was then imaged at high resolution via the use of the inbuilt dual SEM function.

This testing was also performed on conductive inks which had not undergone the ultrasonic encapsulation process. This allowed for a direct comparison to a reference sample in order to establish the effect of the embedding process on the microstructure of the silver inks.

#### 2.5. Effects of circuitry embedment on the mechanical strength of UAM MMC

The effect of circuitry embedment on the mechanical strength of the UAM MMC's formed was identified through a combination of a qualitative method, optical microscopy, and a quantized method, mechanical peel testing.

### 2.5.1 Optical microscopy analysis

Optical microscopy analysis was performed in order to obtain the samples linear weld density (LWD). LWD is defined as the ratio of bonded area along the weld interface to the total length of the interface. This term can be described by the following formula:

$$LWD(\%) = \frac{L_b}{L_i} \times 100 \quad (5)$$

where  $L_b$  and  $L_i$  are the length of bonded area and the total length of weld interface, respectively. This provided a quantised measure of the possible influence of circuitry embedment and UAM embedding energy on the mechanical strength of UAM MMC. The width of the embedment area (WEA) was also measured to obtain the size of the region with no Al-Al bond.

It has been shown previously that aluminium UAM builds are essentially gapless for very high power UAM (VHP-UAM, ~9 kW) [40–43]. However, for protecting vulnerable electrical circuitries traditional UAM apparatus (~2 kW) was used in this work. Moreover, it has been observed in our previous research that the embedding of electrical materials caused a deterioration of LWD due to an increase of voids at the embedding interfaces [30]. These resulting voids lead to stress concentration and degradation of the mechanical properties [44]. Thus, LWD measure was still adopted as a useful indicator of bond quality in this work.

For each type of sliver conductor embedded using a certain UAM energy set, two samples were cross-sectioned and investigated via optical microscopy. Four samples with no embedded circuitry were also capped with both UAM parameter sets and their cross-section investigated as reference. Each sample was cut into front, middle, and rear sections (Fig. 7(a)). The sections were mounted in epoxy resin and then gradually ground and polished to a 0.05 micron finish. In total thirty-six sections were prepared and investigated. A Nikon Eclipse MA200 optical microscope with a  $\times 10$  magnification object lens was employed to image the welding interface for LWD calculations. For each cross-section, eight images were taken from both sides of the embedded circuitry (Fig. 7(b)). The region directly containing the printed structure was excluded from the LWD measurements as this material has been previously shown to play no part in ultrasonic bonding [30]. A  $\times 1$  object lens was used to take images of the embedment areas for WEA measurement.

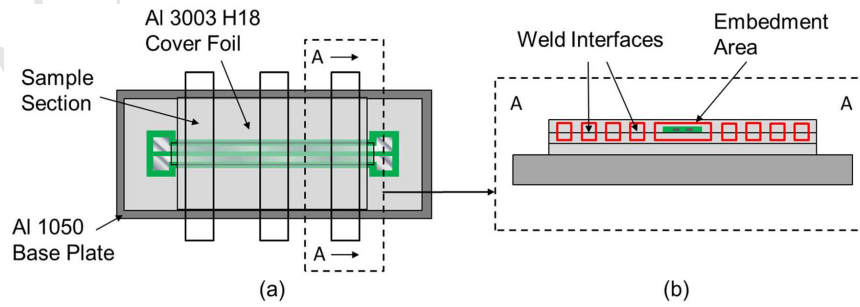


Fig. 7. Method of optical microscopy analysis.

### 2.5.2 Peel testing

The bulk mechanical strength that measures such as ultimate shear strength (USS, the shear plane was along the weld interfaces of the test specimen), transverse tensile strength (TTS, the tensile test force was applied perpendicular to the weld interfaces), and longitudinal tensile strength (LTS, the weld interfaces were parallel to the applied axial force) has been systematically investigated in previous works [45–47]. It has been found that the TTS was typically the weakest strength (~28 MPa) at around 15% of the ultimate tensile strength (UTS) of wrought Al 3003-H18 material. Comparatively, the USS and LTS were 52.7 MPa and 234 MPa, which were approximately 48% and 117% of wrought Al 3003-H18 material [47]. The lowest strength index usually determines the application area of the mechanical components, therefore, transverse tensile strength (i.e. z axis strength) was chosen as the key index in this work for the characterizing the effects of circuitry embedment on the mechanical strength of UAM MMCs. Additionally, a 5 mm thick Al 1050-H14 base plate was used in this work to ensure a flat and stable UAM substrate for the successive electrical circuitry printing process. The unavoidable inclusion of the plate in standardized USS, ULTS and bending measurement tests [45] would have led to false results with regards to the UAM structures strength. Thus peel testing was utilised in this work and performed in accordance with BS EN 2243-2 2005. This method enables quantitative analysis of UAM bond quality via assessing a sample's average resistance to peeling for the particular UAM embedding parameters. By comparing the peeling loads of the samples with and without embedded circuitry, the effects of embedded circuitry and UAM processing energy on mechanical strength could be quantitatively assessed.

As shown in Fig. 8, peeling samples were inserted into a custom peeling jig, and free end of the cover foil was clamped by a chuck. A peeling load was then applied to the chuck through an Instron 5500R tensile test machine (Instron, High Wycombe, UK). For each UAM embedding parameter set, six samples were peeled and the mean values of the maximum peeling loads obtained. Twelve samples with no embedded circuitry were also fabricated using both UAM embedding parameter sets and peeled to measure the mechanical peel strength of the monolithic samples. This method has been heavily utilised in previous works in order to assess interlaminar bond strength in UAM structures [16,48,49]. This is due to the bonding observed in this region being akin to adhesive bonding and peel testing (as opposed to tensile, compressive, shear testing etc.).

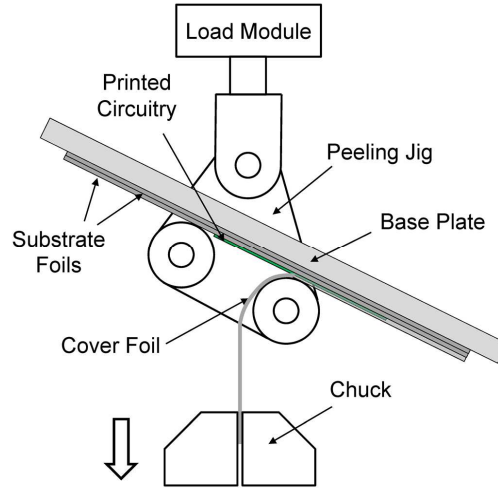


Fig. 8. Schematic drawing of peel testing.

### 3. Results and discussion

#### 3.1. Topography of UAM aluminium substrate and printed circuitry

The topography of UAM aluminium substrates and printed circuitries was investigated using an Alicona InfiniteFocus® G4f as described in section 2.3, and the data was analysed using the systems TalyMap Platinum 5.0 software. Typical surface topographies of unflattened and flattened UAM aluminium substrates are illustrated in Fig. 9, and the profiles of printed circuitry are shown in Fig. 10. The average surface roughness  $S_a$ , the maximum peak-to-valley distance  $R_{z \max}$  of both UAM aluminium substrates and the base insulation layer, and the average thickness of the base insulation layer are stated in Table 2.

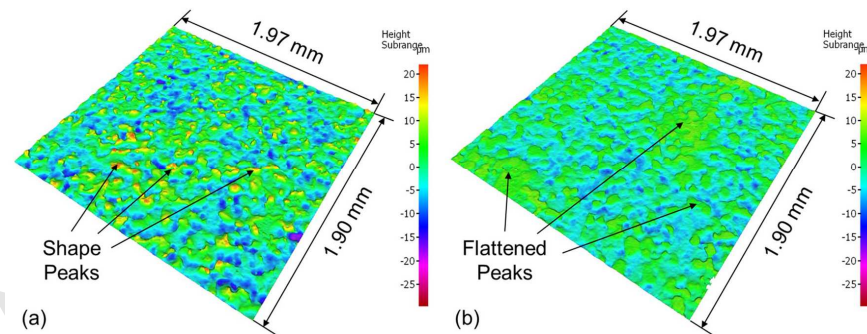


Fig. 9. Surface topographies of unflattened (a) and flattened (b) UAM aluminium substrates.

There was no Ti foil to Al substrate bonding observed after the surface flattening process due to the fact that no ultrasonic oscillation was applied by the sonotrode and the set pressure and speed were insufficient to induce bonding on their own. The Ti foil was thus regarded as a flattening tool only in this process, as opposed to a potential UAM bonding layer.

As Fig. 9(a) demonstrates, on the unflattened substrate there were numerous sharp peaks imparted by the textured sonotrode during UAM welding which could cause short-connections between metal matrices and conductors. After the flattening process, these peaks were deformed leading to smoother top surfaces (Fig. 9(b)). The average surface roughness ( $S_a$ ) of the substrate was reduced from  $3.05 \mu\text{m}$  to  $2.76 \mu\text{m}$ , and the maximum peak-to-valley distance ( $R_z$ ) decreased from  $27.28 \mu\text{m}$  to  $16.24 \mu\text{m}$  (Table 2). Therefore for flattened substrates, a single insulation layer (thickness:  $20.82 \mu\text{m}$ ) was sufficiently thick to overcome the roughness of the UAM processed substrates and provide effective electrical insulation (Fig. 10 (a)). Moreover, compared with the aluminium substrate,  $S_a$  and  $R_{z \max}$  of the base insulation layer was reduced by approximately 50%. Smoother insulation surfaces were desirable for printing silver inks, because continuous conductors could be created with less printing strokes (two strokes were required in this work).

Table 2. Topography of UAM aluminium substrates and base insulation layer.

	Unflattened Substrate	Flattened Substrate	Base Insulation Layer
Mean $S_a$ , [ $\mu\text{m}$ ]	$3.05 \pm 0.29$	$2.76 \pm 0.18$	$1.47 \pm 0.06$
Mean $R_{z \max}$ , [ $\mu\text{m}$ ]	$27.28 \pm 1.66$	$16.24 \pm 1.17$	$7.48 \pm 0.19$
Mean Thickness, [ $\mu\text{m}$ ]	—	—	$20.82 \pm 0.57$

Fig. 10(b) shows the profile of a typical screen printed conductor made from the P58 ink along with a profile of a typical finished circuitry (Fig. 10(c)). After the printing of the encapsulating insulation layer, the average thickness of the circuitry was determined to be  $59.53 \pm 0.46 \mu\text{m}$ . This value was in line with the intended values based upon thickness measurements of the conductive and insulation materials [30]. Many previous works have reported the successful embedding of secondary phase materials with larger diameters/thicknesses than this structure [38,50]. Providing the mechanical properties of the UAM structure are not significantly degraded as a result of the inclusion of this electrical circuit within the interlaminar region (Section 3.3.), this sandwich structure was considered to be highly suitable for embedding based upon its thickness.

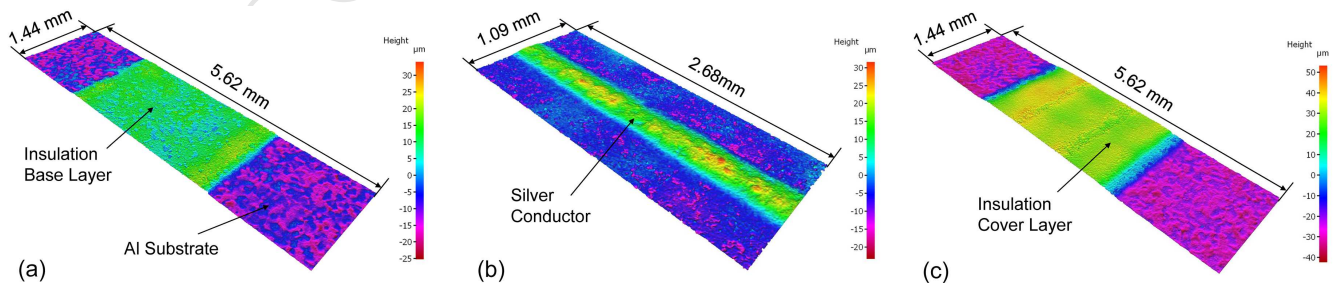


Fig. 10. Typical profiles of the UAM substrate with printed circuitry: (a) insulation base layer; (b) silver conductor (P58 ink); and (c) finished circuitry.

The finished print dimensions of the conductive traces made of two silver inks are located below in Table 3.

Table 3. Measured dimensions of conductive traces prior to embedding

Conductive Ink	Designed Width ( $\mu\text{m}$ )	Actual Width ( $\mu\text{m}$ )	Standard error of width ( $\mu\text{m}$ )	Actual Height ( $\mu\text{m}$ )	Standard error of Height ( $\mu\text{m}$ )
4D3	400	448.1	$\pm 2.6$	27.0	$\pm 0.6$
	500	549.3	$\pm 2.9$	28.8	$\pm 0.8$
P58	400	450.6	$\pm 1.9$	25.1	$\pm 0.4$
	500	551.2	$\pm 1.6$	25.4	$\pm 0.6$

### 3.2. Effects of UAM embedding on the conductivity of printed conductors

#### 3.2.1 Resistivity of printed conductors before and after UAM embedding

The optical microscopy analysis (Fig. 15(a) and (b)) showed that there was no obvious deformation or cracking of the silver conductors after UAM embedding. Thus, the profile data obtained by the Alicona scanning was suitable to be used to calculate the resistivity of the printed conductors before and after UAM embedding. For each width of conductor and each UAM energy set, three samples (six conductors) were investigated, and four-point probe measurement were successfully carried out for all samples both before and after embedding. With the profile data and the resistance of the conductor, the MATLAB<sup>®</sup> program based on Eq. (3) was used to determine the resistivity of the track. The resistivity of 4D3 and P58 silver conductors with standard error are stated in Table 4 and plotted in Fig. 11 and Fig. 12, respectively.

Table 4. The resistivity of 4D3 and P58 silver conductors with standard error.

Line width	Resistivity of 4D3 conductor with standard error ( $\Omega \cdot \text{cm}$ )				Resistivity of P58 conductor with standard error ( $\Omega \cdot \text{cm}$ )			
	Before LE UAM	After LE UAM	Before HE UAM	After HE UAM	Before LE UAM	After LE UAM	Before HE UAM	After HE UAM
400 $\mu\text{m}$	$2.02 \times 10^{-4}$ $\pm 0.06 \times 10^{-4}$	$9.67 \times 10^{-4}$ $\pm 0.65 \times 10^{-4}$	$2.16 \times 10^{-4}$ $\pm 0.04 \times 10^{-4}$	$2.190 \times 10^{-3}$ $\pm 2.58 \times 10^{-4}$	$0.85 \times 10^{-4}$ $\pm 0.06 \times 10^{-4}$	$6.52 \times 10^{-4}$ $\pm 0.35 \times 10^{-4}$	$0.82 \times 10^{-4}$ $\pm 0.04 \times 10^{-4}$	$1.216 \times 10^{-3}$ $\pm 0.93 \times 10^{-4}$
500 $\mu\text{m}$	$2.10 \times 10^{-4}$ $\pm 0.13 \times 10^{-4}$	$9.52 \times 10^{-4}$ $\pm 1.25 \times 10^{-4}$	$2.13 \times 10^{-4}$ $\pm 0.15 \times 10^{-4}$	$2.082 \times 10^{-4}$ $\pm 2.39 \times 10^{-4}$	$0.79 \times 10^{-4}$ $\pm 0.04 \times 10^{-4}$	$6.68 \times 10^{-4}$ $\pm 0.36 \times 10^{-4}$	$0.80 \times 10^{-4}$ $\pm 0.04 \times 10^{-4}$	$1.212 \times 10^{-3}$ $\pm 1.41 \times 10^{-4}$

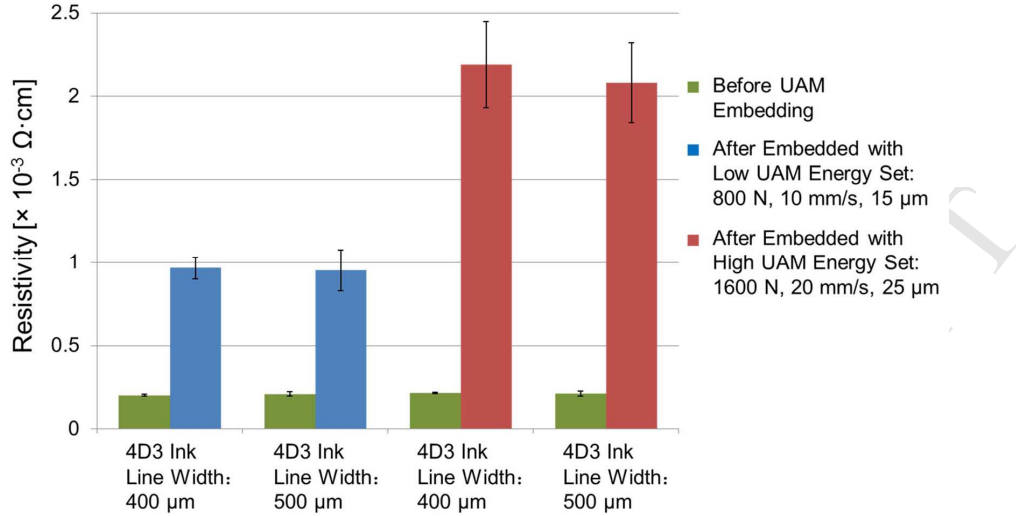


Fig. 11. Resistivity of 4D3 silver conductors before and after UAM embedding.

For all four sample categories, the resistivity of 4D3 conductors before embedding was around  $2.1 \times 10^{-4} \Omega\cdot\text{cm}$ , slightly lower than the value quoted in the manufacturer's manual ( $2.5 \times 10^{-4} \Omega\cdot\text{cm}$ ). Upon the application of the low UAM energy set, for both line width the resistivity of the samples was seen to increase from about  $2.1 \times 10^{-4} \Omega\cdot\text{cm}$  to about  $9.6 \times 10^{-4} \Omega\cdot\text{cm}$ . Following a rise in UAM energy, the average resistivity of embedded samples raised from about  $9.6 \times 10^{-4} \Omega\cdot\text{cm}$  up to about  $2.2 \times 10^{-3} \Omega\cdot\text{cm}$  and exhibited a larger standard error. For 400 μm and 500 μm line width samples, the difference of resistivity after UAM was  $0.15 \times 10^{-4} \Omega\cdot\text{cm}$  for low UAM energy embedding and  $0.1 \times 10^{-3} \Omega\cdot\text{cm}$  for high UAM energy embedding which was considered negligible. Therefore, it can be concluded that the effect of UAM process on the resistivity may not be sensitive to the dimensions of the conductor.

For P58 ink, the general tendency of resistivity was similar to the 4D3 ink. However, P58 presented lower original resistivity, approximately a third of 4D3 value, and after embedding the resistivity increased from  $8 \times 10^{-5} \Omega\cdot\text{cm}$  to  $6.6 \times 10^{-4} \Omega\cdot\text{cm}$  for the low UAM energy and to  $1.2 \times 10^{-3} \Omega\cdot\text{cm}$  for the high UAM energy, respectively. The final resistivity of P58 was 71% and 55% of its 4D3 counterpart for low and high UAM energies. Despite the larger relative increase in resistivity of the P58 ink upon the application of UAM energy (The resistance increase of P58 conductors was 1.8 and 1.4 times larger than 4D3 for low and high UAM energies.), its overall resistivity was demonstrated to be lower than the 4D3 counterpart. As a result, it was considered to be the more suitable ink for use in the embedding of conductive tracks via UAM.

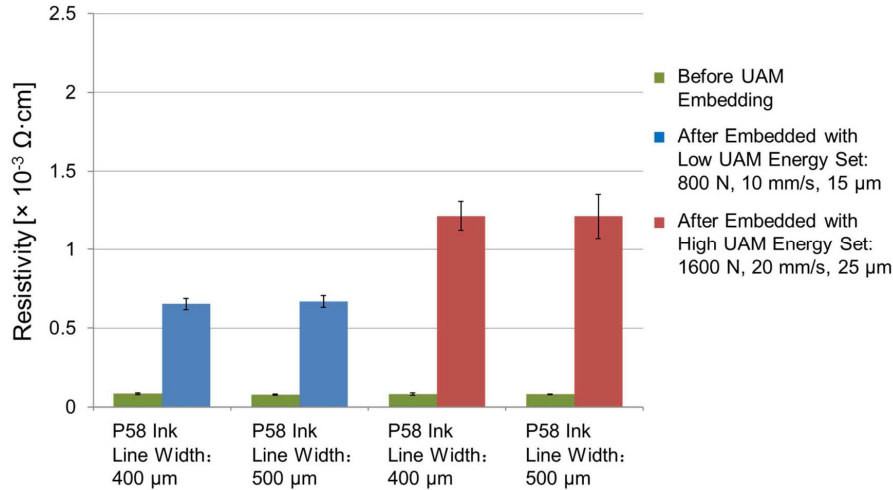


Fig. 12. Resistivity of P58 silver conductors before and after UAM embedding.

### 3.2.2 FIB investigation of silver conductors

With the increase in UAM energy, the degradation of electrical conductivity of both the silver inks became more significant (Fig. 11 and 12). Dual FIB-SEM was used to further investigate potential causes for this resistivity increase as a result of ultrasonic encapsulation. It had been considered that the application of ultrasonic energy to the conductive track may cause the individual particles to agglomerate and form a track with more continuous conductive pathways and therefore lower resistivity. The realisation that this was not the case meant that further investigation was required to establish the root cause of the increase in resistivity.

SEM imaging of trenches milled into the centre of conductive tracks both before and after embedding via UAM indicated that there was no net consolidation of the individual silver particles (Fig. 13). This is indicated by the fact that the overall density/packing of the particles appears to be almost identical both before and after the application of the encapsulating layer. This is likely as a result of the protective insulation layer and the binder in silver ink acting to dampen the ultrasonic energy and mechanical stress of UAM. This prevents these energies and stresses being directly exerted on the fillers contained within the ink. This appears to sufficiently protective so as to prevent any significant cracking of the particles, and this therefore was not considered to be a cause for the increased resistivity.

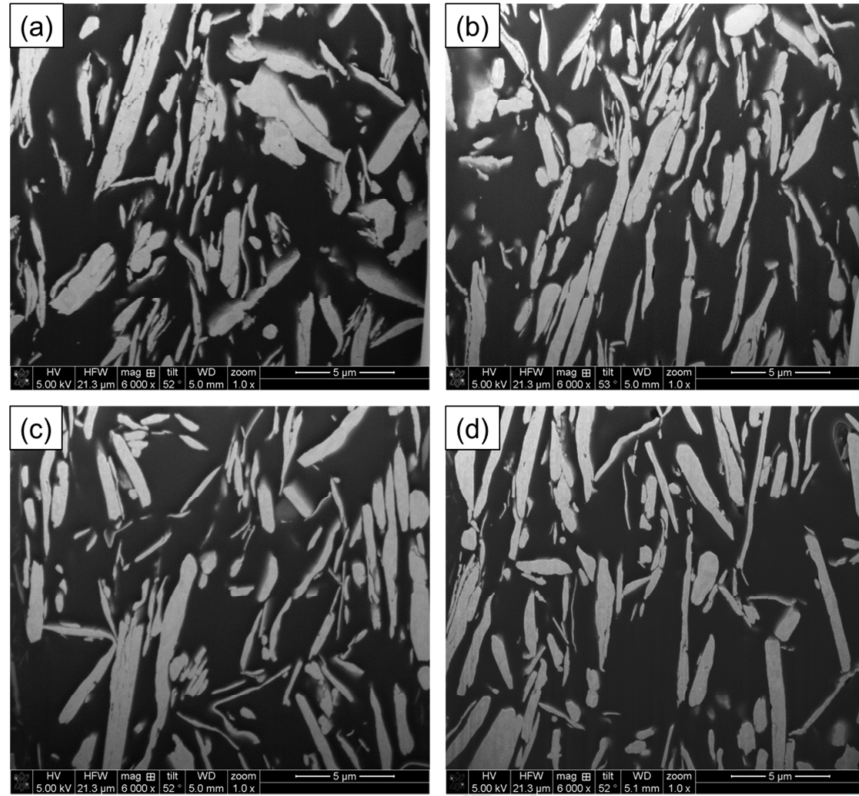


Fig. 13. SEM images of conductive silver inks before and after application of UAM energy: (a) C2131014D3 Silver ink prior to encapsulation; (b) C2131014D3 Silver ink after embedded at higher UAM energy; (c) C2050712P58 Silver ink prior to encapsulation; and (d) C2050712P58 Silver ink after embedded at higher UAM energy.

In order to establish the cause of the resistivity increase, enhanced magnification was used to assess the relationship between the silver particles and the surrounding resin matrix. At magnification levels of  $\times 50,000$ , it was noted that samples encapsulated using applied ultrasonic energy displayed significant dislodging of the particles from the surrounding resin matrix (Fig. 14). This was noted in a number of fillers in these samples for both inks. The effect of this increase in voids around the fillers is a subsequent reduction in the cohesive force felt on the fillers as a result of resin (which contracts during curing to force particles together). This results in less pressure on the contacting points between silver fillers and therefore larger contact resistance along the conductive pathways in the tracks. In turn a higher resistivity is displayed by these samples.

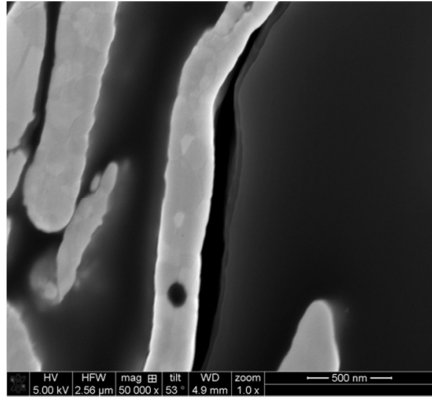


Fig. 14.  $\times 50,000$  magnified SEM images of boundary between conductive silver particles and surrounding resin of C2131014D3 silver ink embedded using high UAM energy.

This void formation may occur as a result of the compression and decompression of the resin material during the application of the covering layer. Optical images taken in Section 3.3.1 indicated that there was no net change in the shape of the electrical structure after embedding (Fig. 15(a) and (b)). The elastic nature of the resin causes it to deform as the sonotrode passes over it and then return to its original geometry after the load is removed. This may cause the void formation as a result of particle movement during compression of the cured resin generating small pockets around them as a result of their movement.

The lower resistivity displayed by the flake filled P58 when compared to its 4D3 counterpart with particle fillers, both before and after UAM embedding, was attributed to the geometry of the particle filler. For the same metal loading percentage, the larger flakes contained within the P58 ink will have a larger surface area and as a result are likely to form more contact spots and thus form more continuous conductive networks [32]. This allows for more electrical pathways to be formed throughout the conductive track when compared to their particle filler counterpart. However it was noted that the P58 inked appeared more sensitive to UAM embedding than 4D3, which caused a greater rate of resistivity increase after UAM embedding. This is likely as a result of the denser conductive networks in this ink potentially being more susceptible to the compressive action of the sonotrode leading to void formation around particle.

### 3.3. Effects of circuitry embedment on the mechanical strength of UAM MMC

#### 3.3.1 Linear weld density (LWD) and width of embedding area (WEA)

Linear welding density (LWD) and width of embedding area (WEA) were obtained via microscopically investigating sample cross-sections as described in section 2.5.2. Fig. 15 (a) and (b) show a typical cross-section of the circuitry embedding area before and after UAM embedding. The printed circuitry with P58 silver conductor was embedded using low UAM energy (Fig. 15 (b)). The sandwich structure of printed circuitry was maintained after UAM embedding and no obvious cracking or squashing was observed in the image. A typical cross-

section of an Al-Al weld area is shown in Fig. 15(c) where some voids were found in the welding interface between the second and third (covering) Al foils.

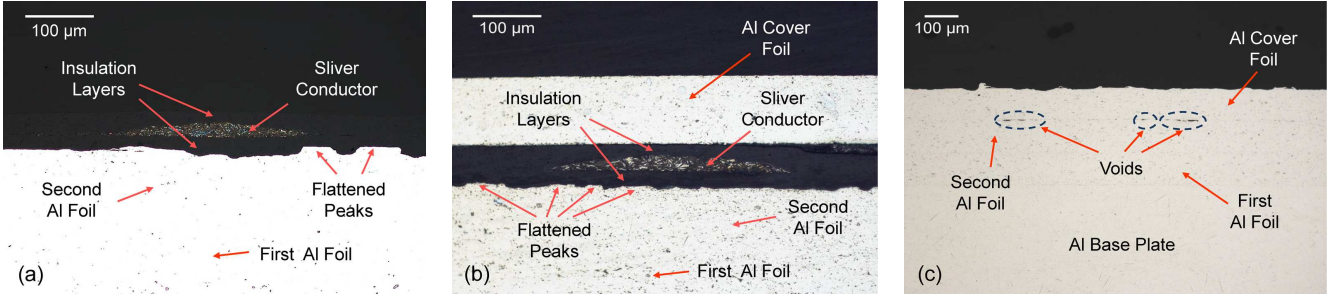


Fig. 15. (a) Cross-section of printed circuitry before embedding; (b) Cross-section of circuitry embedding area; (c) Cross-section of Al-Al weld area.

Fig. 16 shows the average LWD for the samples with and without circuitries encased with two UAM energy sets. Generally, the higher UAM energy set created larger average LWDs for both categories, which agreed with observations from previous research [16,30,35,36]. It was noticeable that for the samples with no circuitry, the low UAM energy set could generate a similar average LWD (around 98%) as the high UAM energy parameters. According to previous research, low UAM parameters could only provide 77% LWD on unflattened substrate whereas high energy set could achieve a LWD of 97% [30]. The different LWD results were attributed to the surface flattening process used in this work. With the decrease of surface roughness, the shallower valleys could be filled with minor plastic flow driven by low UAM energy creating seamless bonding. Moreover, the absence of voids acted to enhance the structural integrity of the structure.

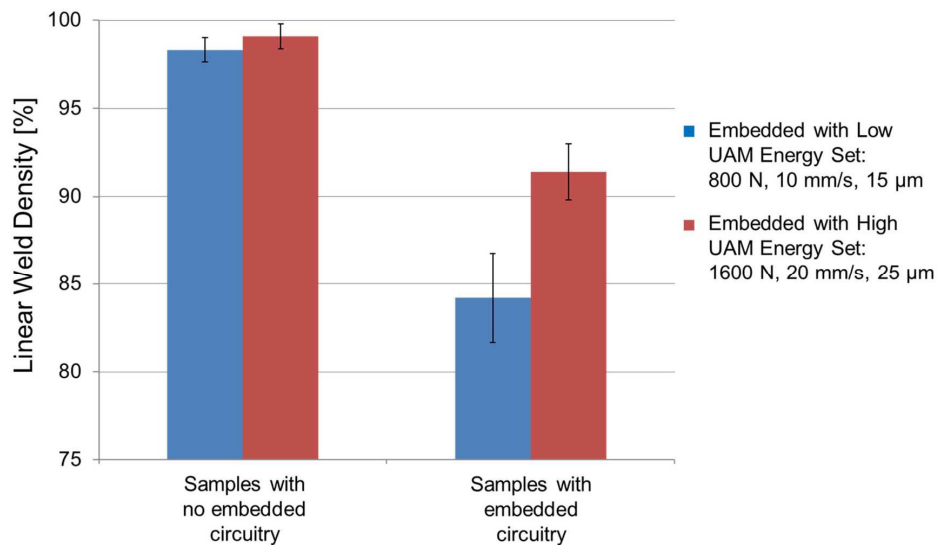


Fig. 16. The average LWD for the samples with and without circuitries embedded with high and low UAM processing energy.

Compared with the samples featuring no embedded circuitry, the LWD of circuitry embedded samples showed a larger standard error and reduced by approximately 8% for high UAM energy and 14% for low UAM energy, respectively. In addition, WEA measurement revealed that the average WEA of the samples with circuitries decreased from  $5.37 \pm 0.14$  mm to  $4.78 \pm 0.14$  mm following the increase of UAM energy. A probable cause of these results was that higher UAM energy generated greater plastic deformation of the Al cover foils, allowing better adaptation to the profile of the circuitries. This acted to minimise the width of the embedment area and simultaneously maintained the average LWD of Al-Al bonding interface either side of the embedded structure.

Due to the realisation that the flattened surface has acted to increase the apparent linear welding density by reducing the degree of plastic flow required to adapt to the topography of the underlying surface, it could be considered that this LWD is even less indicative of the overall bonding strength than is usually seen in UAM work. This means that there are likely to be even more regions of intimate contact without the presence of metal-metal bonding. As a result of this, it was pertinent to therefore also assess the samples resistance to peeling in order to better assess the state of bonding between these layers.

### 3.3.2 Peeling load

As described in section 2.2 and 2.5.2, samples with and without circuitries were embedded via high and low UAM energy welding parameters and their average resistance to peeling determined via mechanical peel testing. The average maximum peeling loads with standard error are plotted in Fig. 17.

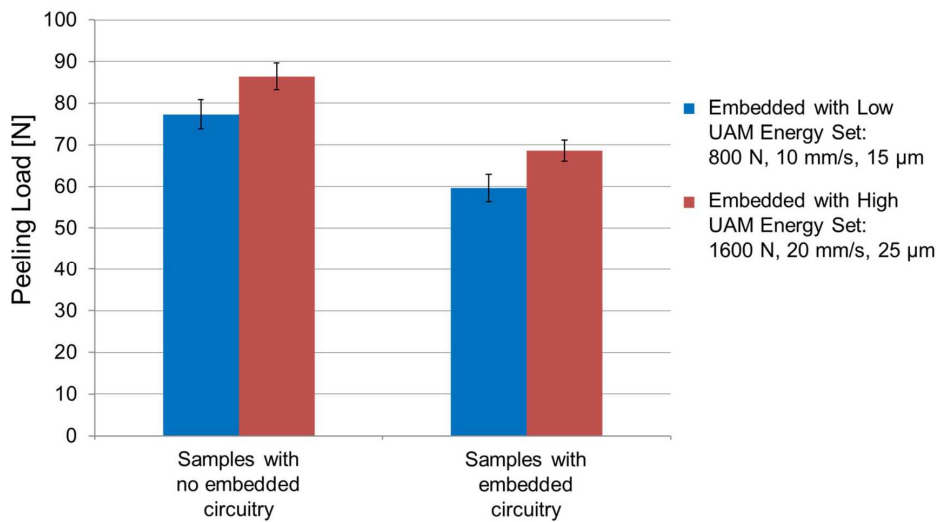


Fig. 17. Peeling loads for the samples with and without circuitries embedded with high and low UAM processing energy.

It is clear that when the printed circuitries were integrated, the peeling load reduced from 86 N to 68 N by ca. 21% for high UAM energy and from 77 N to 60 N by ca. 22% for low UAM energy

parameters, respectively. According to WEA measurement results, the ratios of embedding area over the total welding interface (24 mm in width), were 20% and 22% for high and low UAM embedding energy, respectively, which were in accordance with the decrease rate of the peeling loads. The reduction in peel resistance between samples prepared at LE and HE sets is expected to result due to the lower degrees of plastic flow induced within the matrix at these lower processing energies. This plastic flow is a key driving force for the formation of metallurgical bonds along the welding interface. This plastic flow is also driven in some part by friction at the interface caused by the oscillation of the rough underlying foil with the overlying foil to be welded. This second driving factor had already been significantly reduced in this work by flattening the surface in order to better facilitate the embedding of the electronic structures. By reducing the total UAM energy in the LE parameter samples, this plastic flow was significantly reduced and therefore the degree of true bonding observed is likewise reduced. This leads to fewer bonded regions along the interface and therefore, a lower resistance to peeling. The decrease in peeling strength for samples featuring embedded structures when compared to their monolithic counterparts was attributed to the reduction in available Al-Al bonding area as a result of its inclusion. As these materials can play no part in the metal-metal bonding process, they act to inhibit the total welding area and thereby reduce the strength of the interlaminar region. It is also possible that as a result of the step height of the circuitry (ca. 60  $\mu\text{m}$ ), the degree of intimate contact between the overlying foil and substrate is further reduced either side of the insulation material. It would be impossible to maintain full mechanical strength of a UAM structure in comparison to its monolithic counterpart, when an additional architecture of any significant size is embedded within the interlaminar region.

In a practical sense, reductions in mechanical performance and interlaminar integrity, as seen in the lower UAM energy parameters, are undesirable. However, as the conductivity of the silver inks embedded at the higher UAM energy parameters was considered to be acceptable (especially in the case of the P58 ink), the higher UAM parameters can be used for the future embedding of these conductive inks, and therefore maintain high degrees of mechanical performance.

The increase in UAM energy also brought with it a change in peeling profile for the two parameter sets. Samples encased using high UAM energies exhibited more brittle fractures with cleaner breaks in the covering foil and with shorter tear “teeth” (Fig. 18(a)), while for low UAM energy samples more ductile fractures with longer “teeth” were observed (Fig.18(b)). The density and distribution of the metallic bonding in the welding interface is the main reason for this issue. The ease at which the covering foil was peeled away from the underlying substrate demonstrates that this lower energy processing parameter combination results in: either fewer regions in which the foils are bonded to one another and/or the regions where these samples are bonded are not sufficiently strong enough to negate tear propagation. For higher UAM energy, more metallic bonds were generated and distributed homogeneously in the welding interface, and thus shorter “teeth” and a higher resistance to peeling was observed. Although with surface flattening process low UAM energy could achieve large LWD (Fig. 16), there were

still many areas that only had intimate contacts and a lack of real metallic bonds in the welding interface. Therefore, long “teeth” appeared in these samples under relatively low peeling loads.

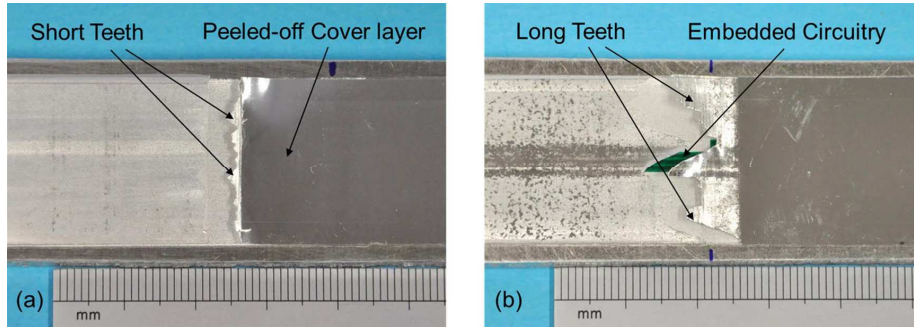


Fig. 18. Two fracture mode of Al cover layer observed in the peel testing: (a) short “teeth”; (b) long “teeth”.

According to optical microscopy analysis and peel testing, higher UAM energy is favourable for maintaining the mechanical strength of UAM MMC’s when printed circuitries were embedded. However, higher UAM energy caused larger conductivity degradation of the conductors. According to Yang’s model [37], UAM processing energy is determined by the combinations of control parameters (normal force, sonotrode amplitude, and welding speed). Future work will look to focus on the effects of each individual control parameter on the conductivity of printed conductors and how they may vary, thus identifying any issues. These parameters may then be optimised to maximize the mechanical strength of MMCs and simultaneously limit the degradation of the conductivity of embedded conductors. Moreover, the decrease of peeling loads mainly depends on the WEAs, therefore an even more effective flattening process, e.g. exerting ultrasonic oscillation on the sonotrode during rolling, could be employed to decrease the surface roughness further and thereby reduce the total thickness of printed circuitry even more. This could also be helpful to decrease WEAs.

#### 4. Conclusions and future work

This work created novel multifunctional metal matrix composites via directly embedding printed electrical circuitries within the interlaminar region of UAM metal matrices. These printed electrical structures required no additional pockets or secondary materials to protect them from the embedding process, and maintained their functionality even after encapsulation at higher UAM energies.

A specific surface flattening process was developed to eliminate the risk of short circuiting between the metal matrices and printed conductors. Furthermore, the total thickness of the printed circuitry could be reduced as a result of this flattening. This acted to improve the integrity of the UAM MMC’s and their resultant mechanical strength. With the protection afforded by the robust 520 Series insulation shell, the conductivity of both silver inks was maintained after UAM embedding, even under relatively high UAM process energy set. The P58 flake filled silver ink demonstrated significantly better conductivity after UAM embedding than its 4D3 particle filled

counterparts, as described by their relative resistivity. The P58 ink was seen to demonstrate a resistivity of  $6.6 \times 10^{-4} \Omega \text{ cm}$  at low embedding energies and  $1.2 \times 10^{-3} \Omega \text{ cm}$  at high embedding energies. In contrast the resistivity of the 4D3 ink measured almost twice these values at  $9.6 \times 10^{-4} \Omega \text{ cm}$  at lower energies and  $2.2 \times 10^{-3} \Omega \text{ cm}$  at high embedding energies. This reduced resistivity and therefore higher conductivity is desirable for practical applications which will be explored in later work.

The mechanical strength of the UAM MMC's was investigated via peel testing and microscopy. It was found that mechanical strength of MMC could be enhanced by applying higher UAM embedding energy which when combined with the novel surface flattening process used in this work acted to improve the linear weld density (LWD) of MMC. This enhanced the structural integrity and mechanical strength of the structure. This increased UAM energy was however noted to result in a subsequent increase in the resistivity of the embedded conductive materials (by ca.  $5.4 \times 10^{-4} \Omega \text{ cm}$  for P58 ink and  $1.24 \times 10^{-3} \Omega \text{ cm}$  for 4D3 ink). Even at these higher parameters, the conductivity is still sufficient for a wide array of potential applications.

Reductions in peeling loads through the reduction in UAM embedding energies was attributed to reductions in plastic flow and reduced friction at the welding interface, whilst reductions as a result of the inclusion of embedded materials was attributed to reduced available Al-Al bonding areas. This second factor was demonstrated as being the most significant as it brought about a reduction of approximately 20 N for the peel resistance in samples with embedded structures compared to their monolithic equivalents whereas the UAM energy change resulted in an approximately 10 N reduction.

In order to realise the freeform integration of electrical circuitry within metal matrix composites, future work will focus on the embedment of printed circuitries in a 3D manner (i.e. in the z axis, perpendicular to the layup process). This work will enable a wide range of potential applications to be explored such as smart metal components with fully embedded printed sensors, actuators, and even micro- and nanoelectromechanical systems (MEMS and NEMS) [51–59].

### Acknowledgement

This work was supported by the Engineering and Physical Sciences Research Council, UK via the Centre for Innovative Manufacturing in Additive Manufacturing, grant number EP/I033335/2. We thank Mr. Jagpal Singh from the Metrology Laboratory and Mr. Scott Doak from Loughborough Materials Characterisation Centre (LMCC) at Loughborough University for their support on topology measurement and FIB-SEM investigation, respectively.

### Reference

- [1] Weiss LE, Prinz FB, Neplotnik G, Padmanabhan P, Schultz L, Merz R. Shape deposition manufacturing of wearable computers. Proc. 1996 Solid Free. Fabr. Symp., 1996, p. 10–2.

- [2] Weiss LE, Merz R, Prinz FB, Neplotnik G, Padmanabhan P, Schultz L, et al. Shape deposition manufacturing of heterogeneous structures. *J Manuf Syst* 1997;16:239–48. doi:10.1016/S0278-6125(97)89095-4.
- [3] Prinz FB, Weiss LE. Novel Applications and Implementations of Shape Deposition Manufacturing. *Nav Res Rev* 1998;50:19–26.
- [4] Medina F, Lopes A, Inamdar A, Hennessey R, Palmer J, Chavez B, et al. Hybrid Manufacturing: Integrating Direct-Write and Stereolithography. *Proc. 2005 Solid Free. Fabr. Symp.*, 2005, p. 39–49.
- [5] Lopes A, Navarrete M, Medina F, Palmer J, MacDonald E, Wicker R. Expanding Rapid Prototyping for Electronic Systems Integration of Arbitrary Form. *Proc. 2006 Solid Free. Fabr. Symp.*, 2006, p. 644–55.
- [6] De Nava E, Navarrete M, Lopes A, Alawneh M, Contreras M, Muse D, et al. Three-Dimensional Off-Axis Component Placement and Routing for Electronics Integration using Solid Freeform Fabrication. *Proc. 19th Annu. Solid Free. Fabr. Symp.*, 2008, p. 362–9.
- [7] MacDonald E, Salas R, Espalin D, Perez M, Aguilera E, Muse D, et al. 3D printing for the rapid prototyping of structural electronics. *IEEE Access* 2014;2:234–42. doi:10.1109/ACCESS.2014.2311810.
- [8] Espalin D, Muse DW, MacDonald E, Wicker RB. 3D Printing multifunctionality: Structures with electronics. *Int J Adv Manuf Technol* 2014;72:963–78. doi:10.1007/s00170-014-5717-7.
- [9] Li X, Johnson J, Groza J, Prinz F. Processing and microstructures of fiber bragg grating sensors embedded in stainless steel. *Metall Mater Trans A* 2002;33:3019–24. doi:10.1007/s11661-002-0286-z.
- [10] Li X, Prinz F. Metal Embedded Fiber Bragg Grating Sensors in Layered Manufacturing. *J Manuf Sci Eng* 2003;125:577–85. doi:10.1115/1.1581889.
- [11] Li X, Tang W, Golnas A. Embedding and characterization of fiber-optic and thin-film sensors in metallic structures. *Sens Rev* 2004;24:370–7. doi:10.1108/02602280410558403.
- [12] Maier RRJ, Havermann D, MacPherson WN, Hand DP. Embedding metallic jacketed fused silica fibres into stainless steel using additive layer manufacturing technology. *Proc. SPIE - Int. Soc. Opt. Eng.*, 2013, p. 87942U. doi:10.1117/12.2026076.
- [13] Friel RJ. Power ultrasonics for additive manufacturing and consolidating of materials. *Power Ultrason. Appl. High-Intensity Ultrasound*, Elsevier; 2014, p. 313–35. doi:10.1016/B978-1-78242-028-6.00013-2.
- [14] White DR. Ultrasonic Consolidation of Aluminium Tooling. *Adv Mater Process* 2003;161:64–5.
- [15] Kong CY, Soar RC, Dickens PM. A model for weld strength in ultrasonically consolidated components. *Proc Inst Mech Eng Part C J Mech Eng Sci* 2005;219:83–91. doi:10.1243/095440605X8315.
- [16] Kong CY, Soar RC, Dickens PM. Optimum process parameters for ultrasonic consolidation of 3003 aluminium. *J Mater Process Technol* 2004;146:181–7. doi:10.1016/j.jmatprotec.2003.10.016.
- [17] Koellhoffer S, Gillespie JW, Advani SG, Bogetti TA. Role of friction on the thermal development in ultrasonically consolidated aluminum foils and composites. *J Mater Process Technol* 2011;211:1864–77. doi:10.1016/j.jmatprotec.2011.06.011.
- [18] Yang Y, Janaki Ram GD, Stucker BE. Bond formation and fiber embedment during ultrasonic consolidation. *J Mater Process Technol* 2009;209:4915–24. doi:10.1016/j.jmatprotec.2009.01.014.

- [19] Kong CY, Soar RC, Dickens PM. Ultrasonic consolidation for embedding SMA fibres within aluminium matrices. *Compos Struct* 2004;66:421–7. doi:10.1016/j.compstruct.2004.04.064.
- [20] Dapino M. Additive Manufacturing of Smart Metallic Structures 2012:2–4. doi:10.1117/2.1201401.005322.
- [21] Hahnlen R, Dapino MJ. Active Metal-matrix Composites with Embedded Smart Materials by Ultrasonic Additive Manufacturing. *Proc SPIE - Int Soc Opt Eng* 2010;7645:76450O–76450O–12. doi:10.1117/12.848853.
- [22] Dapino MJ. Smart Structure Integration Through Ultrasonic Additive Manufacturing 2014;2:1–8. doi:10.1115/SMASIS20147710.
- [23] Mou C, Saffari P, Li D, Zhou K, Zhang L, Soar R, et al. Smart structure sensors based on embedded fibre Bragg grating arrays in aluminium alloy matrix by ultrasonic consolidation. *Meas Sci Technol* 2009;20:34013. doi:10.1088/0957-0233/20/3/034013.
- [24] Kong CY, Soar R. Method for embedding optical fibers in an aluminum matrix by ultrasonic consolidation. *Appl Opt* 2005;44:6325–33. doi:10.1364/AO.44.006325.
- [25] Siggard EJ, Madhusoodanan a. S, Stucker BE, Eames B. Structurally Embedded Electrical Systems Using Ultrasonic Consolidation (UC). *Proc. 17th Solid Free. Fabr. Symp.*, 2006, p. 70–83.
- [26] Robinson CJ, Stucker B, Lopes AJ, Wicker RB, Palmer JA. Integration of direct-write (DW) and ultrasonic consolidation (UC) technologies to create advanced structures with embedded electrical circuitry. *Proc. 17th Annu. Solid Free. Fabr. Symp. Univ. Texas Austin, Austin, TX, Society of Manufacturing Engineers*; 2006, p. 60–9.
- [27] Hopkins CD, Foster D, Dapino MJ, Zhang L, Aerospace D. Metal-matrix composite metamaterials with smart switches embedded by ultrasonic consolidation. *ASME 2010 Conf. Smart Mater. Adapt. Struct. Intell. Syst. SMASIS 2010*, vol. 2, 2010, p. 471–80.
- [28] Masurtschak S, Friel RJ, Gillner A, Ryll J, Harris RA. Laser-Machined Microchannel Effect on Microstructure and Oxide Formation of an Ultrasonically Processed Aluminum Alloy. *J Eng Mater Technol* 2014;137:11006. doi:10.1115/1.4028926.
- [29] Technic Company. 520 SERIES Thermal 2 Pack Solder Resists. Tech Data Sheet 2008.
- [30] Li J, Monaghan T, Masurtschak S, Bournias-Varotsis A, Friel RJ, Harris RA. Exploring the mechanical strength of additively manufactured metal structures with embedded electrical materials. *Mater Sci Eng A* 2015;639:474–81. doi:10.1016/j.msea.2015.05.019.
- [31] Li Y, Wong CP. Recent advances of conductive adhesives as a lead-free alternative in electronic packaging: Materials, processing, reliability and applications. *Mater Sci Eng R Reports* 2006;51:1–35. doi:10.1016/j.mser.2006.01.001.
- [32] Li Y, Lu D, Wong CP. Electrical conductive adhesives with nanotechnologies. Springer; 2010. doi:10.1007/978-0-387-88783-8.
- [33] Gwent Group. C2131014D3 Flexible Silver Ink. Tech Data Sheet 2011.
- [34] Gwent Group. C2050712P58 Curable Silver Paste. Tech Data Sheet 2013.
- [35] Janaki Ram GD, Yang Y, Stucker BE. Effect of process parameters on bond formation during ultrasonic consolidation of aluminum alloy 3003. *J Manuf Syst* 2006;25:221–38. doi:10.1016/S0278-6125(07)80011-2.
- [36] Kulakov M, Rack HJ. Control of 3003-H18 Aluminum Ultrasonic Consolidation. *J Eng Mater Technol* 2009;131:21006. doi:10.1115/1.3078303.
- [37] Yang Y, Janaki Ram GD, Stucker BE. An analytical energy model for metal foil deposition in ultrasonic consolidation. *Rapid Prototyp J* 2010;16:20–8. doi:10.1108/13552541011011668.

- [38] Monaghan T, Capel a. J, Christie SD, Harris R a., Friel RJ. Solid-State Additive Manufacturing for Metallized Optical Fiber Integration. *Compos Part A Appl Sci Manuf* 2015;76:181–93. doi:10.1016/j.compositesa.2015.05.032.
- [39] Fischler M a., Bolles RC. Random sample consensus: a paradigm for model fitting with applications to image analysis and automated cartography. *Commun ACM* 1981;24:381–95. doi:10.1145/358669.358692.
- [40] Sojiphan K, Sriraman MR, Babu SS. Stability of microstructure in Al3003 builds made by very high power ultrasonic additive manufacturing. *Proc. 2010 Solid Free. Symp.*, 2010, p. 362–71.
- [41] Wolcott PJ, Hehr A, Pawlowski C, Dapino MJ. Process improvements and characterization of ultrasonic additive manufactured structures. *J Mater Process Technol* 2016;233:44–52. doi:10.1016/j.jmatprotec.2016.02.009.
- [42] Wolcott PJ, Hehr A, Dapino MJ. Optimized welding parameters for Al 6061 ultrasonic additive manufactured structures. *J Mater Res* 2014;29:2055–65. doi:10.1557/jmr.2014.139.
- [43] Fujii HT, Sriraman MR, Babu SS. Quantitative evaluation of bulk and interface microstructures in Al-3003 alloy builds made by very high power ultrasonic additive manufacturing. *Metall Mater Trans A Phys Metall Mater Sci* 2011;42:4045–55. doi:10.1007/s11661-011-0805-x.
- [44] Janaki Ram GD, Yang Y, Stucker BE. Effect of process parameters on bond formation during ultrasonic consolidation of aluminum alloy 3003. *J Manuf Syst* 2006;25:221–38. doi:10.1016/S0278-6125(07)80011-2.
- [45] Yang Y, Stucker BE, Janaki Ram GD. Mechanical Properties and Microstructures of SiC Fiber-reinforced Metal Matrix Composites Made Using Ultrasonic Consolidation. *J Compos Mater* 2010;44:3179–94. doi:10.1177/0021998310371528.
- [46] Hahnlen R, Dapino MJ, Short M, Graff K. Aluminum-matrix composites with embedded Ni-Ti wires by ultrasonic consolidation. *Proc SPIE* 2009;7290:729009-729009–12. doi:10.1117/12.817036.
- [47] Schick DE, Hahnlen RM, Dehoff R, Collins P, Babu SS, Dapino MJ, et al. Microstructural characterization of bonding interfaces in Aluminum 3003 blocks fabricated by ultrasonic additive manufacturing. *Weld J* 2010;89:105–15.
- [48] Kong CY, Soar RC, Dickens PM. Characterisation of aluminium alloy 6061 for the ultrasonic consolidation process. *Mater Sci Eng A* 2003;363:99–106. doi:10.1016/S0921-5093(03)00590-2.
- [49] Yang Y, Stucker B, Ram G. Mechanical properties and microstructures of SiC fiber-reinforced metal matrix composites made using ultrasonic consolidation. *J Compos Mater* 2010.
- [50] Kong CY, Soar R. Method for embedding optical fibers in an aluminum matrix by ultrasonic consolidation. *Appl Opt* 2005;44:6325. doi:10.1364/AO.44.006325.
- [51] Fu Y, Du H, Huang W, Zhang S, Hu M. TiNi-based thin films in MEMS applications: A review. *Sensors Actuators, A Phys* 2004;112:395–408. doi:10.1016/j.sna.2004.02.019.
- [52] Lee Z, Ophus C, Fischer LM, Nelson-Fitzpatrick N, Westra KL, Evoy S, et al. Metallic NEMS components fabricated from nanocomposite Al-Mo films. *Nanotechnology* 2006;17:3063–70. doi:10.1088/0957-4484/17/12/042.
- [53] Li M, Tang HX, Roukes ML. Ultra-sensitive NEMS-based cantilevers for sensing, scanned probe and very high-frequency applications. *Nat Nanotechnol* 2007;2:114–20. doi:10.1038/nnano.2006.208.
- [54] Apuzzo A, Barretta R, Canadija M, Feo L, Luciano R, Sciarra FM De. A closed-form model for torsion of nanobeams with an enhanced nonlocal formulation. *Compos Part B* 2016;108:315–24. doi:10.1016/j.compositesb.2016.09.012.

- [55] Barretta R, Feo L, Luciano R, Marotti de Sciarra F. A gradient Eringen model for functionally graded nanorods. *Compos Struct* 2015;131:1124–31.  
doi:10.1016/j.compstruct.2015.06.077.
- [56] Barretta R, Feo L, Luciano R, Marotti de Sciarra F. An Eringen-like model for Timoshenko nanobeams. *Compos Struct* 2016;139:104–10.  
doi:10.1016/j.compstruct.2015.11.048.
- [57] Barretta R, Feo L, Luciano R, Marotti De Sciarra F. Application of an enhanced version of the Eringen differential model to nanotechnology. *Compos Part B Eng* 2016;96:274–80. doi:10.1016/j.compositesb.2016.04.023.
- [58] Barretta R, Feo L, Luciano R, Marotti de Sciarra F, Penna R. Functionally graded Timoshenko nanobeams: A novel nonlocal gradient formulation. *Compos Part B Eng* 2016;100:208–19. doi:10.1016/j.compositesb.2016.05.052.
- [59] Barretta R, Luciano R, Sciarra FM De. A Fully Gradient Model for Euler-Bernoulli Nanobeams 2015;2015.